Measurement of di-electron anisotropy for strong magnetic field search in Cu+Cu collisions at $\sqrt{s_{NN}} = 200$ GeV at PHENIX

Tomoya Hoshino (M110713)

Quark Physics Laboratory
Department of Physics
Graduate School of Science
Hiroshima University

Supervisor: Associate Prof. Kenta Shigaki
Primary examiner: Associate Prof. Kenta Shigaki
Examiner: Associate Prof. Tsunefumi Mizuno

February 28th, 2013

Abstract

Strong magnetic field is created in heavy ion collisions. This intense magnetic field is caused by non-central collisions of high energy nuclei, for example gold or copper, in highly narrow space, about $10fm$. And the maximum strength amounts to 10^{14} $tesla$ at the energy region of the Relativistic Heavy Ion Collider(RHIC). This strength is higher than Magnetar that is a type of neutron star with extremely intense magnetic field, 10^{11} $tesla$. This magnetic field strength and space-time evolution is calculated by some theoretical models.

Strong field physics is attracted because this has very interesting physics such as vacuum birefringence, Schwinger mechanism and synchrotron radiation of quarks. Strong magnetic field physics is mainly researched by theoretical side, but it had not detected in any experimental research. Thus, experimental confirmation of strong magnetic field in heavy ion collisions is really important and meaningful. This thesis is pioneering measurement of di-electron anisotropy and porlarization for magnetic field search in heavy ion collisions.

Creation of magnetic filed in heavy ion collisions is appeared in the primary stage of collisions. And this strong field can have effect on decay of photons and its yield of azimuth dependence and polarization. In addition, since photons and leptons are not operated by strong interaction, these are good probe to detect this strong magnetic field's effects.

In this thesis, Cu+Cu 200 GeV Minimum Bias data set is used because this is one of the best data set in PHENIX to analyze with di-electron analysis. In this analysis, asymmetry of di-electrons with respect to the reaction plane and porlarization are showed. One is asymmetry of number of electron pairs, it is like elliptic flow. And another is polarization, it means that di-electron opening angle correlation with reaction plane. Moreover centrality dependence of these anisotropy and polarization are shown and discussed these plots for the purpose of strong magnetic field search.

In conclusion, we measured anisotropy and polarization of di-electron for selected centralities and selected mass region. The measured di-electron anisotropy is consistent with the calculated anisotropy using elliptic flow (v2). We measure two di-electron polarization, one is the polarization for reaction plane side, and the other is for magnetic field side. In order to cancel detector acceptance, we used double ratio using both side polarization. The double ratio value are consistent with unity in error bar.

Contents

List of Figures

List of Tables

1 Introduction

1.1 Relativistic heavy ion collisions

High-energy heavy-ion collision experiment is the only way to reproduce the Quark-Gluon Plasma. The Quark-Gluon Plasma(QGP) is the new phase in quantum chromodynamics(QCD) phase diagram. This phase only exists at extremely high temperature and high energy density. In QGP phase, quarks and gluons are released from nucleons. To research on the nature of QGP, the Relativistic Heavy Ion Collider was constructed at Brookhaven National Laboratory(the United States of America).

RHIC provides collisions of heavy ion, such as gold and copper, at the center of mass energy per nucleon($\sqrt{s_{NN}}$) up to 200 GeV and proton at the center of mass energy($\sqrt{s}$) up to 500 GeV. The Pioneering High Energy Nuclear Interaction eXperiment(PHENIX) is the one of four experiment in RHIC. PHENIX is specialized for the measurement of leptons and photons.

1.2 The strong magnetic field in heavy ion collisions

The possibility of creation of the strong magnetic field in non-central heavy-ion collisions is discussed in about 30 years ago. The pioneering theoretical work [1] estimated the strength of magnetic field in heavy ion collisions. In recent years, the strong magnetic field in heavy ion collisions is noted and discussed the space-time evolution of the magnetic field and physics phenomena in the field, for example vacuum birefringence [**?**], synchrotron radiation, spitting and chiral magnetic effect [4].

The strength of created magnetic field in heavy ion collision is estimated about $10^{18} Gauss$ at the energy region of RHIC. This strength is stronger than magnetars one and this is thought the strongest magnetic field in the universe. Table 1 shows the comparison with the strength of some magnetic fields.

The principle of the magnetic filed creation in heavy ion collisions is very primitive. Strength of magnetic fields created by charged particles can be described by Lienard-Wiechert equation.

$$\overrightarrow{\mathrm{B}}(\overrightarrow{\mathrm{r}}, t) = \frac{e}{4\pi} \frac{[\overrightarrow{\mathrm{v}} \times \overrightarrow{R}]}{cR^3} \frac{(1 - \overrightarrow{\mathrm{v}^2}/c^2)}{[1 - (v/c)^2 \sin^2 \phi_{Rv}]^{3/2}}. \tag{1}$$

Here $\overrightarrow{R} = \overrightarrow{r} - \overrightarrow{r'}$ and ϕ_{Rv} is the angle between $\overrightarrow{R}$ and $\overrightarrow{v}$.

In heavy ion collisions, charged particles (nucleus) are accelerated to light speed and collided with nucleus in very narrow space, about 10 fm. This is the reason why the strong magnetic field is created.

Strength [*Gauss*]	Realized as
0.6	The Earth's magnetic field
100	A typical hand-held magnet
8.3×10^4	Super conducting magnets in LHC
4.5×10^5	Strongest-steady artificial magnets
$\sim 10^{12}$	Magnetic filed on surface of the neutron stars
4×10^{13}	Critical magnetic field of electrons
$\sim 10^{15}$	Magnetic filed on surface of the magnetars
$\sim 10^{18}$	Non-central heavy-ion collisions at $\sqrt{s_{NN}} = 200$GeV (RHIC)
$\sim 10^{19}$	Non-central heavy-ion collisions at $\sqrt{s_{NN}} = 5.5$TeV (LHC)

Table 1: Comparison with the strength of magnetic fields

The magnetic field in heavy ion collisions is very strong and it has very interesting physics. However the field is not yet directly detected in experiments.

1.3 Time evolutions

In this section, time evolution of heavy ion collisions are described. Figure 1.1 shows the space-time evolution in heavy ion collisions at RHIC.

1.3.1 Time evolution of heavy ion collisions

Time evolution of high-energy heavy-ion collisions is explained step by step in this section.

Pre equilibrium: $\tau = 0 \sim \tau_0$

Accelarated to an energy of 200 GeV per nucleon that they are Lorentz contracted in longitudinal directions and it looks like pan-cakes shape in the lab frame. They are collided in narrow space and create patrons and gluons. It becomes local thermal-equilibrium state shortly.

QGP in thermal equilibrium: $\tau = \tau_0 \sim \tau_C$

After that, thermal-equilibrium state transforms to QGP phase (phase transition). QGP phase can be described by hydrodynamics. QGP is expanding and lowering the heat.

Mixed phase between QGP and hadrons: $\tau = \tau_C \sim \tau_H$

When surpass the critical temperature, hadronization become.

Hadron gas: $\tau = \tau_H \sim \tau_F$

The temperature lower the heat as the system expands. Finally, QGP phase transforms to hadron phase.

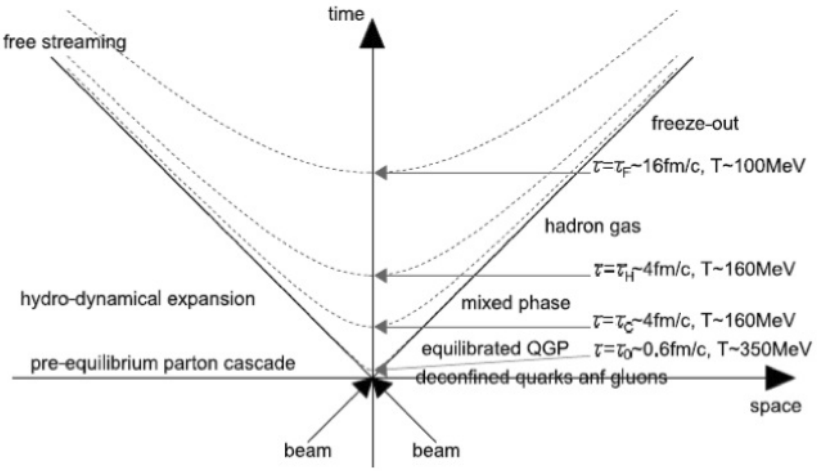

Figure 1.1: Time evolution of heavy ion collisions [3]

1.3.2 Time evolution of the magnetic field

Time evolution of the magnetic field is explained step by step in this section.

Figure 1.2 shows time evolution of the magnetic field in heavy ion collisions that is estimated by one theoretical model. The strength of magnetic field is the strongest at the moment of collision and it is rapidly decreasing. Its time evolution shows this magnetic field is dominant in the pre-equilibrium region and still very strong even after a few fm. Thus This QGP

is formed in the strong magnetic field and the primary stage of QGP can be influenced by the field.

On the one hand, QGP is a marked in central collisions, on the other hand, the strength of magnetic field is a marked in non-central collisions($\sim$ centrality 60%). In addition, electro-magnetic probes such as electrons and photons are adequate for the search of the magnetic field, because their probes are not operated by the strong interaction. Therefore the measurement electromagnetic probes used is to know the preceding stage of QGP state and its evolution.

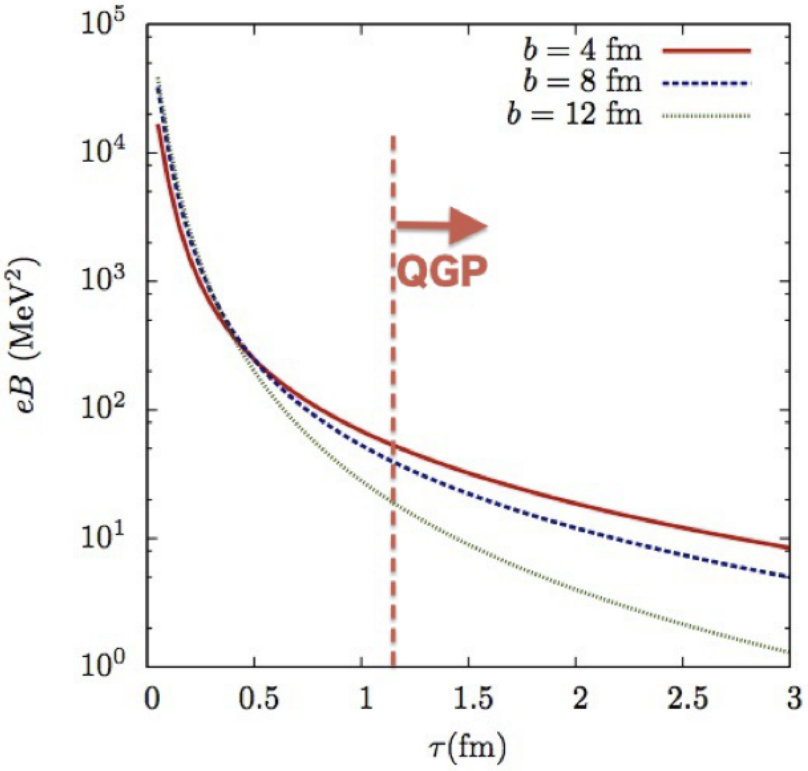

Figure 1.2: Time evolution of the magnetic field [4]

1.4 Photons and leptons

Leptons and photons are very good probe to search the magnetic field in heavy ion collisions because they are not interact with strong interaction which is dominant in QGP phase. Thus these probes are expected to have informations of the magnetic field even after hadronization.

New approaches to detect the field are discussed in recent years. According to calculation of vacuum polarization tensor, virtual photons (low mass di-electrons e^+e^-) have anisotropy and polarization with respect to the reaction plane.

Figure 1.3 is a schematic image of the field in heavy ion collisions and it shows decays of virtual photons to di-electrons. Virtual photons which move parallel to reaction plane are affected by the magnetic field. Thus the number of electron pairs asymmetry between the magnetic field and reaction plane occur and they are polarized when they move perpendicular to the magnetic field.

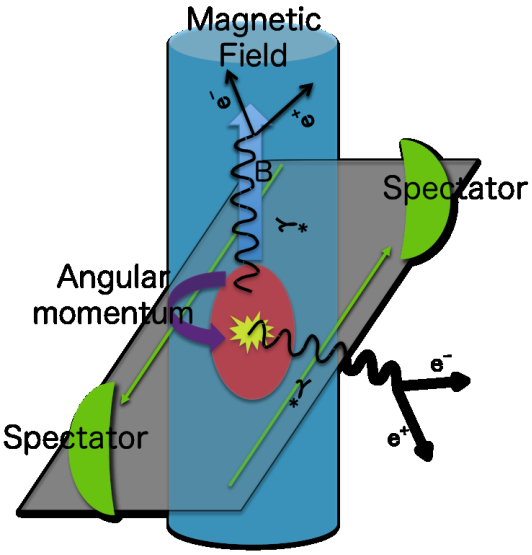

Figure 1.3: Schematic image of strong magnetic field in heavy ion collision and decay of di-electrons from virtual photons.

2 Experimental setup

In this section, the RHIC accelerator, the PHENIX experiment and its detectors are described.

2.1 The RHIC accelerator

The Relativistic Heavy Ion Collider(RHIC) in Brookhave National Laboratory(BNL) in the United States was built to research the high energy heavy ion physics (Fig.2.1).

The maximum energy of RHIC is 100 GeV per nucleon for heavy ion and that is 250 GeV for proton. The heavy ions and protons produced at the source are accelerated at Tandem Van de Graaff and LINAC, respectively, and injected into the Booster. The Booster accelerate them up to 95 MeV per nucleon. They are transported to the Alternating Gradient Synchrotron(AGS) and more accelerated to 8.86 GeV. After that, heavy ions and protons are injected to RHIC.

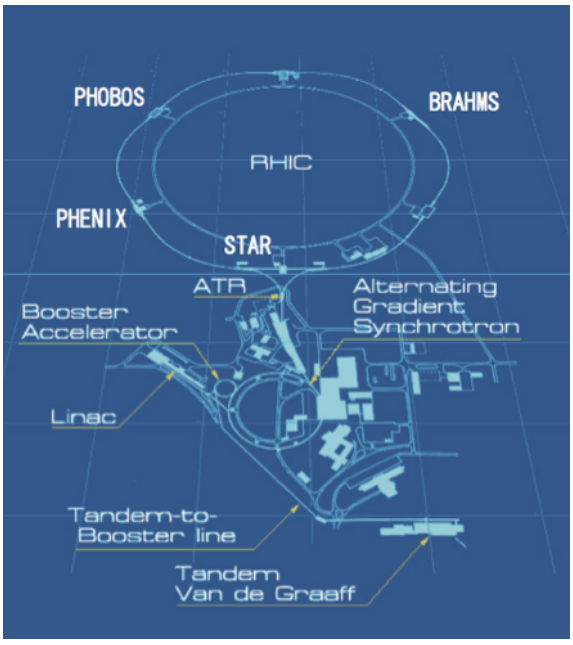

Figure 2.1: Relativistic Heavy Ion Collider(RHIC) complex [5]

The RHIC ring has a circumference of 3.8 km and consists of two rings, one("Blue Ring") for clockwise and the other("Yellow Ring") for counter-clockwise. These rings cross at six interaction points and experiments such as PHENIX and STAR are build in each one of six points.

2.2 The PHENIX experiment

The PHENIX detector is described at Fig.2.2. The PHENIX, Pioneering High Energy Nuclear Interaction eXperiment, is one of the experiment in RHIC collider. The PHENIX detector are composed of global detectors and central arm detectors. And this experiment is specialized for measurement of leptons and photons.

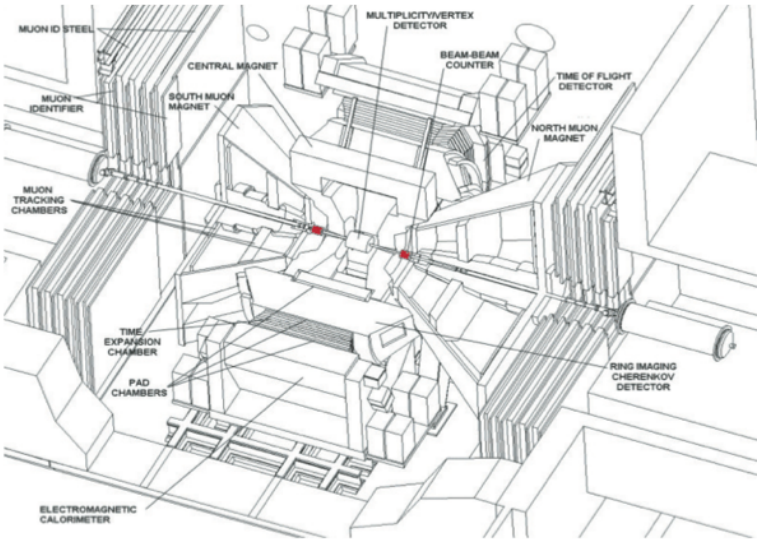

Figure 2.2: Overview of the PHENIX Detector [6]

The PHENIX experiment is a detector system which consists of three detector group. First, central arm, two central arms have $|\eta| < 0.35$ pseudo-rapidity coverage and 180° azimuthal angle. Second, two muon arms, north and south arm cover $1.15 < \eta < 2.44$ and $-1.15 > \eta > -2.45$, respectively, and both are covering full azimuth 2π. The last, global detectors, these are located near the beam pipe.

2.3 Grobal detectors

In this section, the globe detectors such as BBC and ZDC are described. The main purpose of global detectors is make triggers and to measure the luminosity and centrality in heavy ion collisions.

2.3.1 Beam-Beam Counters(BBC)

The Beam-Beam counters(BBC) are one of the PHENIX global detector(Fig.2.3). This detectors located on north and south side at 144.35cm along beam pipe from the collision point and covers the pseude-rapidity frm 3.0 to 3.9. Each of BBC is composed of 64 quartz Cherenkov counters. BBC have following five major tasks; 1) to trigger the Minimum Bias events, 2) to measure the collision vertex, 3) to obtain the collision time, 4) to determine centrality, 5) to determine reaction plane.

The collision time and vertex are determined by the average time and difference to BBC North and South:

$$\text{collision time} = \frac{T_{South} + T_{North} - (2 \times L)/c}{2} \tag{2}$$

$$\text{collision vertex} = \frac{T_{South} - T_{North}}{2} \times c \tag{3}$$

where T_{South} and T_{North} are the average hit time, c is the light velocity and L is the distance between $z = 0$ and both BBCs, $L = 144.35$ cm.

Figure 2.3: Beam Beam Counter [7]

2.3.2 Zero Degree Calorimeters(ZDC)

The Zero Degree Calorimeters(ZDC) are hadron calorimeter which are located at 18 m north and south side along beam pipe from the collision point(Fig.2.4). Since both ZDCs are located at charged particles are deflected by the DX dipole magnet, only neutrons hit the ZDCs. The tasks of ZDCs are to measure the energy of spectator neutrons and to monitor the beam luminosity.

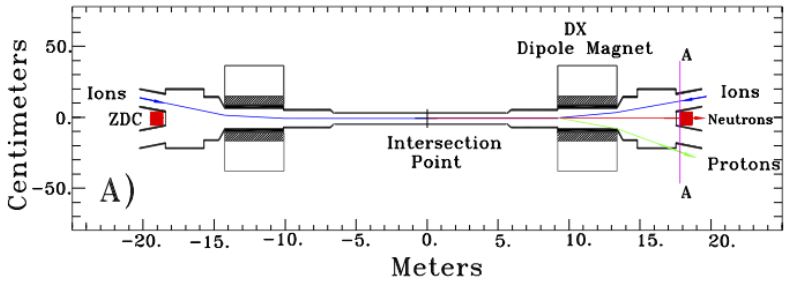

Figure 2.4: Schematic view of the location of Zero Degree Calorimeters [8]

2.4 PHENIX Magnets

PHENIX has two type magnets; One is Central Magnet and the other is Muon Magnets(North and South side). The Central Magnet provides a magnetic field around the collision point. The momentum of charged particle is determined by the bending of their track in this magnetic field. The Central Magnet covers a polar angle range of $70^\circ < \theta < 110^\circ$ and pseudo-rapidity range of $|\eta| < 0.35$.

The Central Magnet consists of inner and outer Helmholtz coil. Both magnets can be operated with the same(++) or opposite(+−) polarity. The magnetic field is 1.15 Tesla in the same polarity configuration. In the opposite polarity configuration, it leads to a cancellation of the magnetic field to about zero field integral inside of 50 cm around the vertex.

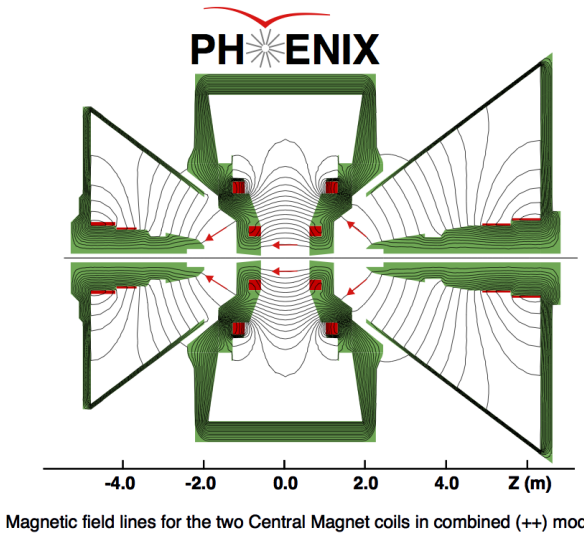

Figure 2.5: The PHENIX Central and Muon Magnets [9]

2.5 Central arm detectors

In this section, detectors in central arms are described. The central arm detectors measure for charged particles tracking, particle identification and their momentum. They cover $|\phi| < \pi/2$ of azimuth angle and $|\eta| < 0.35$ of pseudo-rapidity.

2.5.1 Ring Imaging Cherenkov Counter(RICH)

The Ring Imaging Cherenkov Counter(RICH) is detector for identifying with electrons and positrons. Charged particles traveling in a medium with a velocity βc and when these are greater than the speed of light in the medium, Cherenkov radiation is emitted under angle $\cos\theta = 1/n\beta$. The RICH detector provides discrimination between electrons and pions by using their difference Cherenkov threshold.

Fig.**??** is shown a cut through view of RICH detector in PHENIX. Cherenkov light produced in the radiator gas(CO_2) are focused and reflected on two spherical mirrors and are detected by each photon multiplier tubes(PMTs).

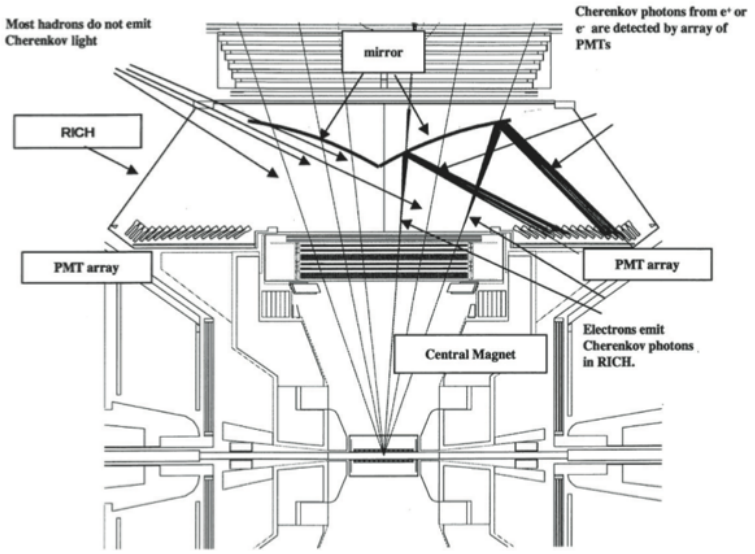

Figure 2.6: A cut through view of RICH detector [10]

2.5.2 Electro-Magnetic Calorimeter (EMCal)

The Electro-Magnetic Calorimeter(EMCal) measures the energy and position of photons and electrons. In addition, The EMCal serves as trigger on rare events with high momentum photons and electrons. The EMCal consists of two type calorimeter, one is the lead-scintillator(PbSc) calorimeter and the other is lead-glass(PbGl) calorimeter. The PbSc provides six sectors for all four sector in the West Arm and for the two top sector in East Arm. And the PbGl provides two sectors for the bottom sector in the East Arm.

The PbSc is a sampleing calorimeter made of alternating tile of Pb and scintillator as shown in Fig.2.7. This calorimeter contains a total if 15,552 individual towers. The energy resolution of the PbSc is $\frac{\sigma_E}{E} = \frac{8.1\%}{\sqrt{E}} \oplus 2.1\%$.

The PbGl is a Cherenkov type calorimeter which made of lead glass. The PbGl calorimeter comprises 192 super modules(SMs) and each SM comprises 24 modules. Fig.2.8 shows the interior view if one super module of PbGl calorimeter. The energy resolution of the PbGl is $\frac{\sigma_E}{E} = \frac{5.9\%}{\sqrt{E}} \oplus 0.76\%$.

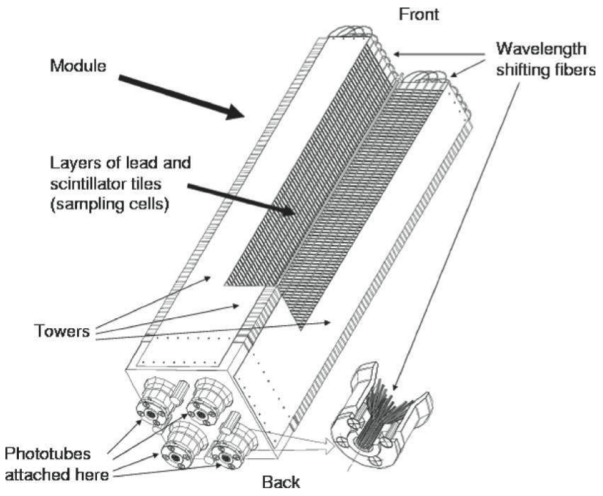

Figure 2.7: View of a lead-scintillator module [11]

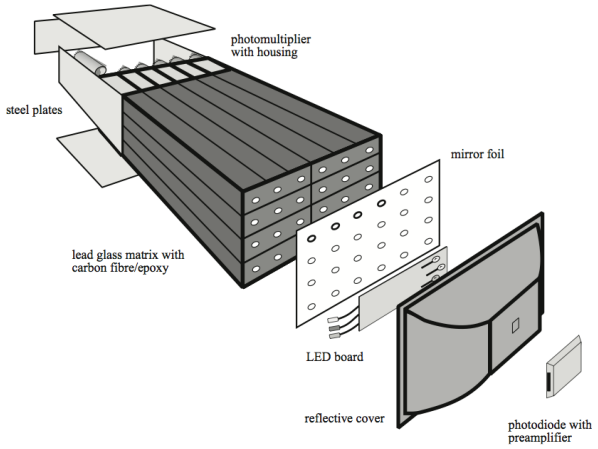

Figure 2.8: View of a lead-glass super module [11]

2.5.3 Drift Chamber (DC)

The Drift Chambers(DCs) are covering both Central Arms. This detector is the main tracking device for charged particles in PHENIX. The DCs reconstruct the tracking of charged particles in $r - \phi$ plane in order to determine transverse momentum of each particles. The Wast and West DCs are covering $|\eta| = \pm 0.35$ in pseudo-rapidity, $-\frac{3}{16}\pi < \phi < \frac{5}{16}\pi$ and $\frac{11}{16}\pi < \phi < \frac{19}{16}\pi$ in azimuth, respectively. The detectors are filled with mixed gas of 50% Argon and 50% Ethane.

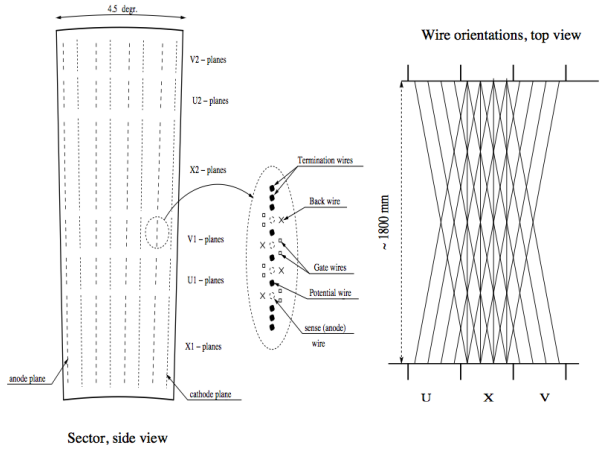

Figure 2.9: The layout of wire position of Drift Chamber [12]

2.5.4 Pad Chamber (PC)

The Pad Chambers(PCs) are multi-wire promotional chambers. This detectors consists of two cathode pad readout. The PCs determine space point along the straight trajectory of charged particles in oder to determine polar angle θ which allows to determine the z component of the momentum vector.

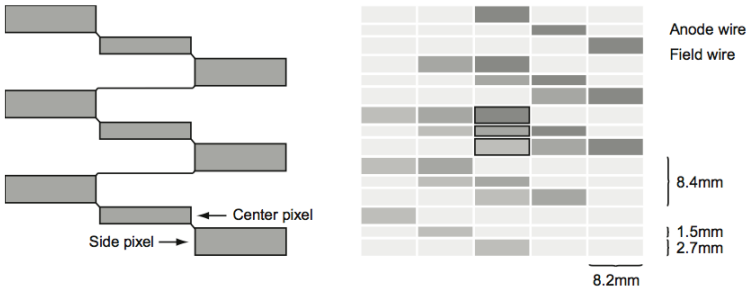

Figure 2.10: The layout of wire position of Drift Chamber [12]

3 Analysis

3.1 Run and event selection

In this section, some basic information on this analysis such as data sets, run and track selection variables and analysis used runs are described.

3.1.1 Data sets

Minimum Bias data set in Cu+Cu collisions at $\sqrt{s_{NN}} = 200$ GeV are used in this analysis. This data set is collected in year 2005 at PHENIX. The run number in Cu+Cu collisions is from to . All runs are separated into two different groups as ++ field and −− field runs. In this analysis, ++ field (magnetic field on) data set are used that consists of 264 runs.

3.1.2 Global cuts

The following global cuts are used in order to select events that used in this analysis.

- Zvertex

  -25 < zvtx < 25 cm

  Zvertex means the collision points.

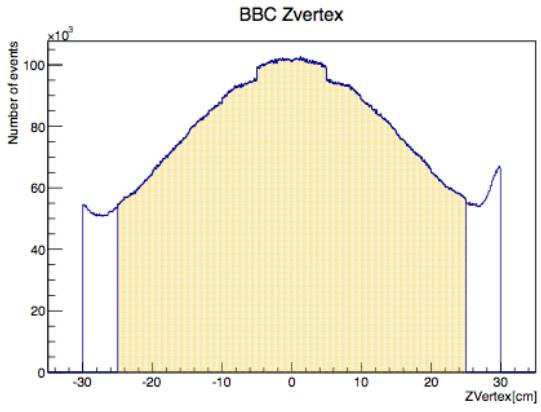

Figure 3.1: ZVertex distribution measured by BBC

- Track quality

  dc quality == 31 or 51 or 63

  This parameter is Drift Chamber tracks quality. The value of 31 means the tracks are required the hit of X1, X2 wire and unique hit of UV wire. The value of 51 means the tracks are

- Fiducial cuts

  -1.37 < phi0 < 1 || 2.14 < phi0 < 4.51

  This cut remove the region of the MVD service pipes in order to reject conversion electrons. $phi0$ is the track's ϕ direction at the vertex.

3.1.3 Centrality determination

Copper nuclei are not point-like particle. Thus, in heavy ion collisions, the center of each two nuclei are shifted by a distance that called the impact parameters $\overrightarrow{b}$ as showed Fig.3.2. Centrality is decided by charge sum detected by the BBC detectors.

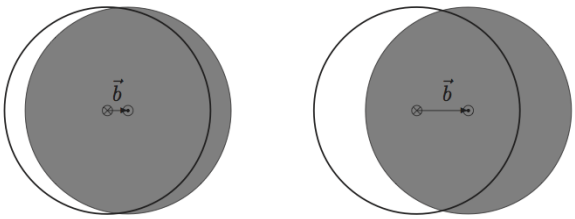

Figure 3.2: Impact Parameter

3.1.4 Reaction Plane determination

Reaction Plane $\Psi_{rp}(n)$ is defined the following equation.

$$\Psi_{rp}(n) = \frac{1}{n}\left(\tan^{-1}\frac{\sum_i \omega_i \sin n\phi_i}{\sum_i \omega_i \cos n\phi_i}\right) \tag{4}$$

Here ω_i is the charged sum detected in azimuthal angle ϕ_i. Figure 3.4 shows the Reaction Plane distribution measured by BBC.

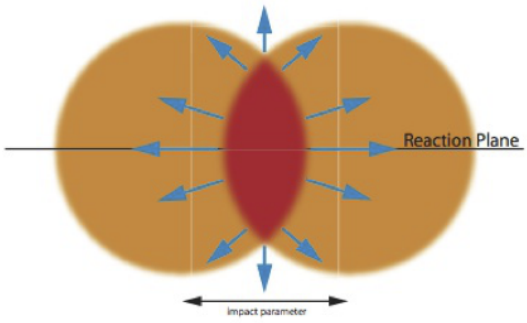

Figure 3.3: Reaction plane and almond shape in non-central collision

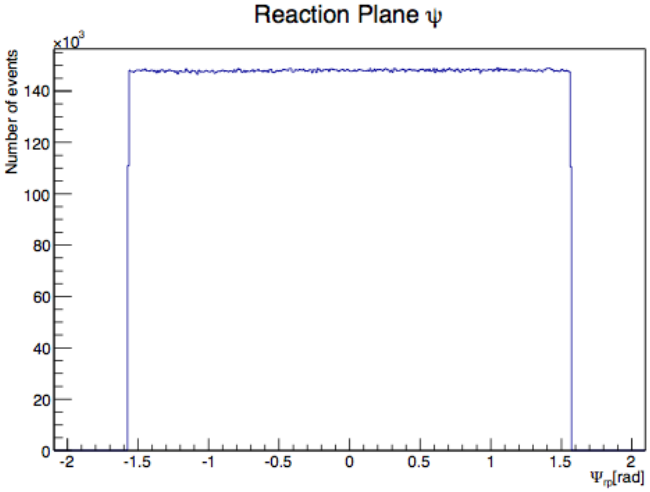

Figure 3.4: Ψ_{rp} distribution measured by BBC

3.1.5 Electron identification

The cut parameters are used in order to identify electrons and positrons.

- RICH

  2 > n0

  The $n0$ is the number of fired phototubes in nominal ring radius.

  χ^2**/npe0** $\geq$ **25**

  χ^2-like shape variable of the RICH ring associated with the track divided by the benumbed of photo-electrons(npe0).

  disp $\leq$**5**

  The *disp* is the displacement between the ring center reconstructed from the fired phototubes and the track projection position in the RICH phototubes array.

- EMCal

  prob > 0.01

  This *prob* parameter is the probability that the particle shower is Electromagnetic.

  0.5 $\leq$ **ecore/mom** $\leq$ **2.0**

  The *ecore* is the shower core energy detected at EMCal and the *mom* is the magnitude of the momentum detected at Drift Chamber.

  $\sqrt{emcsdphi_e^2 + emcsdz_e^2} \leq$ **4.0**

  The $emcsdphi_e$ is track matching in ϕ direction at EMCal surface and the $emcsdz_z$ is track track matching in z direction at EMCal surface.

3.1.6 Pair selection

In order to select di-electrons, the following cut variables are used.

- p_T threshold

  $p_T \geq 0.3$ GeV/c

  This cut parameter is single electron transverse momentum (p_T) threshold.

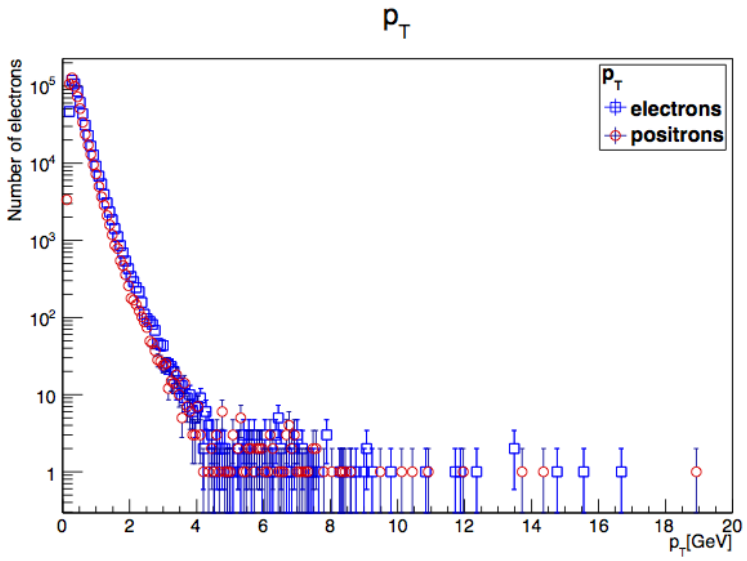

Figure 3.5: Electrons/Positrons transverse momentum distribution

- DC ghost track cut

  $|\Delta dc_{phi}| \geq 0.02$ && $|\Delta dc_{zed}| \geq 0.5$

  This cut is applied to reject ghost tracks in Drift Chamber. If any two tracks fulfill above region, the one with worse EMCal matching is rejection, because it is likely to be a ghost track.

- RICH ring sharing rejection

  $|\Delta cross_{phi}| \geq 0.01$ && $|\Delta cross_{z}| \geq 25$

  This cut is applied in order to reject a hadron. When two tracks are parallel to each other while traveling through the RICH gas, they share the same Cherenkov ring. In this case, one of them is most likely a misidentified hadron. Thus, such tracks should be rejected.

- $\phi_v cut$

  The pairs from gamma conversions can be identified by their orientation angles relative to the PHENIX magnetic field called as ϕ_v. This cut is used in order to reject beam pipe conversions and it can be remove $> 98\%$ of all conversions pairs.

The ϕ_v cut can be described as follows equations.

$$\overrightarrow{u} = \frac{\overrightarrow{p}_{e-} + \overrightarrow{p}_{e+}}{|\overrightarrow{p}_{e-} + \overrightarrow{p}_{e+}|} \tag{5}$$

$$\overrightarrow{v} = \overrightarrow{p}_{e-} \times \overrightarrow{p}_{e+} \tag{6}$$

$$\overrightarrow{\omega} = \overrightarrow{u} \times \overrightarrow{v} \tag{7}$$

$$\overrightarrow{e_z} = (0, 0, 1) \tag{8}$$

$$\overrightarrow{u_a} = \frac{\overrightarrow{u} \times \overrightarrow{e_z}}{|\overrightarrow{u} \times \overrightarrow{e_z}|} \tag{9}$$

$$\phi_v = \arccos\left(\frac{\overrightarrow{\omega} \cdot \overrightarrow{u_a}}{|\overrightarrow{\omega}||\overrightarrow{u_a}|}\right) \tag{10}$$

Here $\overrightarrow{p}_{e-}$ and $\overrightarrow{p}_{e+}$ are 3-momentum vector of electron and positron, respectvely. And e_z is a unit vector correctional with z axis.

The applied ϕ_v cut parameters that is used in this analysis are following(Table. 2).

Mass region [MeV]	$\phi_v cut[rad]$
$0 < M_{ee} \leq 10$	No cut
$10 < M_{ee} \leq 30$	$\phi_v \geq 0.08\ \pi$
$30 < M_{ee} \leq 90$	$\phi_v \geq 0.035\ \pi$
$90 < M_{ee} \leq 140$	$\phi_v \geq 0.03\ \pi$
$140 < M_{ee}$	$\phi_v \geq 0.02\ \pi$

Table 2: ϕ_v cut parameters

3.2 Invariant mass

The invariant mass $M_{e^+e^-}$ is calculated by following equation.

$$M_{e^+e^-} = \sqrt{(E_{e^+} + E_{e^-})^2 - (\overrightarrow{p}_{e+} + \overrightarrow{p}_{e-})^2} \tag{11}$$

where E is the energy of particle and $\overrightarrow{p}$ is particle momentum.

$$(E_{e^+} + E_{e^-})^2 = (\sqrt{m_{e^+}^2 + \overrightarrow{p}_{e^+}^2} + \sqrt{m_{e^-}^2 + \overrightarrow{p}_{e^-}^2})^2 \tag{12}$$

$$\overrightarrow{p}_{e^+} = (p_{e^+x}, p_{e^+y}, p_{e^+z}) \tag{13}$$

$$\overrightarrow{p}_{e^-} = (p_{e^-x}, p_{e^-y}, p_{e^-z}) \tag{14}$$

The invariant e^+e^- mass distribution showed in fig.3.6. In this anisotropy and polarization analysis, $0.12 < M_{ee} < 0.3GeV/c^2$ is used because this region is include about 20% virtual photon component.

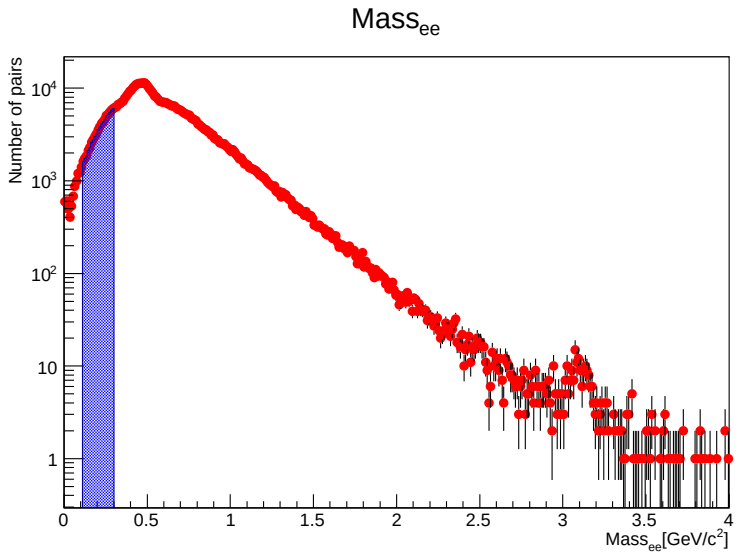

Figure 3.6: Invariant e^+e^- mass spectrum. The blue band is $0.12 < M_{ee} < 0.3GeV/c^2$. This region is include about 20% virtual photon component.

3.3 Anisotropy

The anisotropy is calculated by the following equations.

First, two electrons momentum are added. This vector means the direction of di-electron in XY plane.

$$\overrightarrow{P}_{e^-e^+}\big|_{xy} = \overrightarrow{P}_{e^-} + \overrightarrow{P}_{e^+} \tag{15}$$

Second, in order to determine the reaction plane in XY plane, the reaction plane vector is defined.

$$\overrightarrow{P}_{rp}\big|_{xy} = (\cos\Psi_{rp}, \sin\Psi_{rp}) \tag{16}$$

Third, the angle of between these two vectors $\overrightarrow{P}_{e^-e^+}$ and $\overrightarrow{P}_{rp}$ are measured.

$$\cos\varphi_{anisotropy} = \frac{\overrightarrow{P}_{e^-e^+} \cdot \overrightarrow{P}_{rp}}{|\overrightarrow{P}_{e^-e^+}||\overrightarrow{P}_{rp}|} \tag{17}$$

$$\varphi_{anisotropy} = \arccos\varphi_{anisotropy} \tag{18}$$

- $0 \leq \varphi_{anisotropy} < \frac{1}{4}\pi$ and $\frac{3}{4}\pi < \varphi_{anisotropy} \leq \pi$

  The electron pairs are in in-plane. This means the momentum of di-electrons direction are reaction plane.

- $\frac{1}{4}\pi \leq \varphi_{anisotropy} < \frac{3}{4}\pi$

  The electron pairs are in out-plane. This means the momentum of di-electrons direction are magnetic field.

Finally, the number of electron pairs are compared between in-plane and out-plane. The anisotropy is defined as follows:

$$Anisotropy = \frac{N_{RP} - N_{MF}}{N_{RP} + N_{MF}} \tag{19}$$

N_{RP} and N_{MF} are the number of electron pairs in the reaction plane side and the magnetic field side, respectively.

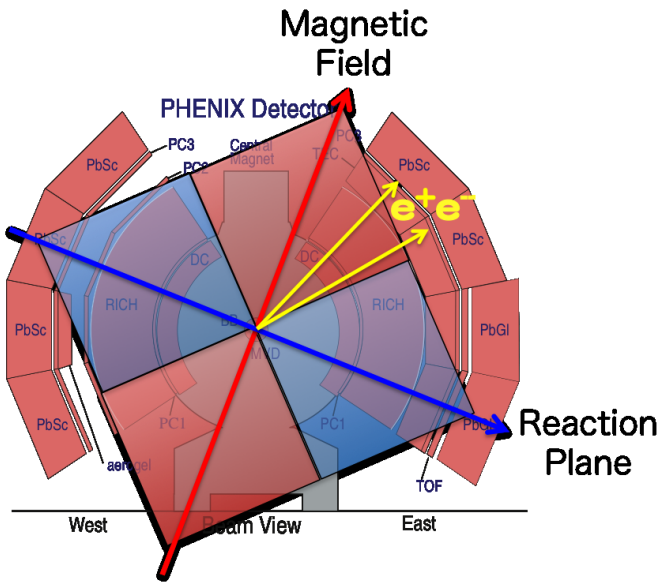

Figure 3.7: Schematic image of RP(reaction plane) and MF(magnetic field) region

3.4 Polarization

The polarization is calculated by the following equations.

First, the 3-momentum vector which is the perpendicular to the momentum vector of electron and positron are defined.

$$\overrightarrow{P}_e = \overrightarrow{P}_{e^-} \times \overrightarrow{P}_{e^+} \tag{20}$$

Second, the vector of magnetic field is defined by using Ψ_{rp} and unit vector of the z axis.

$$\overrightarrow{P}_{rp} = (\cos\Psi_{rp}, \sin\Psi_{rp}, 0) \tag{21}$$

$$\overrightarrow{P}_{mf} = \overrightarrow{P}_{rp} \times \overrightarrow{e}_z \tag{22}$$

Third, calculate the angle between $\overrightarrow{P}_e$ and $\overrightarrow{P}_{mf}$. It means the angle between two plane, reaction plane and "electron pair plane". This value is used for the polarization of in-plane electron pair.

$$\cos\varphi_{polarization_{RP}} = \frac{\overrightarrow{P}_e \cdot \overrightarrow{P}_{mf}}{|\overrightarrow{P}_e||\overrightarrow{P}_{mf}|} \tag{23}$$

$$\varphi_{polarization_{RP}} = \arccos\varphi_{polarization_{RP}} \tag{24}$$

For the calculation of the polarization of out-plane electron pairs, the following angle are used. This means that the angle between "electron pair plane" and the plane which is composed by magnetic field and z unit vector.

$$\cos\varphi_{polarization_{MF}} = \frac{\overrightarrow{P}_e \cdot \overrightarrow{P}_{rp}}{|\overrightarrow{P}_e||\overrightarrow{P}_{rp}|} \tag{25}$$

$$\varphi_{polarization_{MF}} = \arccos\varphi_{polarization_{MF}} \tag{26}$$

- $0 \leq \varphi_{polarization} < \frac{1}{4}\pi$ and $\frac{3}{4}\pi < \varphi_{polarization} \leq \pi$

  This $\varphi_{polarization}$ region means that di-electron momentum vector is parallel to the reaction plane for in-plane polarization or magnetic field for out-plane polarization.

- $\frac{1}{4}\pi \leq \varphi_{polarization} < \frac{3}{4}\pi$

  This $\varphi_{polarization}$ region means that di-electron momentum vector is perpendicular to the reaction plane for in-plane polarization or magnetic field for out-plane polarization.

The number of electron pairs are compared between the parallel and perpendicular plane to the reaction plane(magnetic field).

$$Polarization_{RP} = \left(\frac{N_\parallel - N_\perp}{N_\parallel + N_\perp}\right)_{RP} \tag{27}$$

$$Polarization_{MF} = \left(\frac{N_\parallel - N_\perp}{N_\parallel + N_\perp}\right)_{MF} \tag{28}$$

Finally, the double ratio is calculated with the double ratio of the both side polarization.

$$D.R = \left(\frac{N_\parallel - N_\perp}{N_\parallel + N_\perp}\right)_{RP} \Bigg/ \left(\frac{N_\parallel - N_\perp}{N_\parallel + N_\perp}\right)_{MF} \tag{29}$$

This is because in order to cancelation of detector geometrical acceptance.

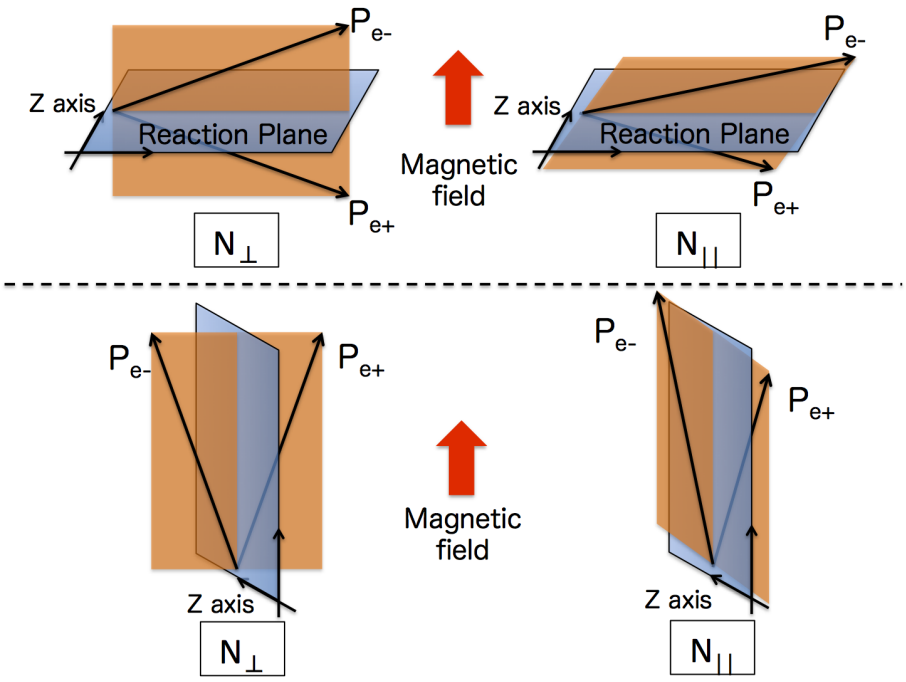

Figure 3.8: Definition of polarization analysis

4 Results and Discussion

In this section, the results of anisotropy and polarization are showed.

4.1 Anisotropy

4.1.1 Comparison with different mass region

The anisotropy as a function of centrality is showed in Figure 4.1. The plot is zero consistent within error range.

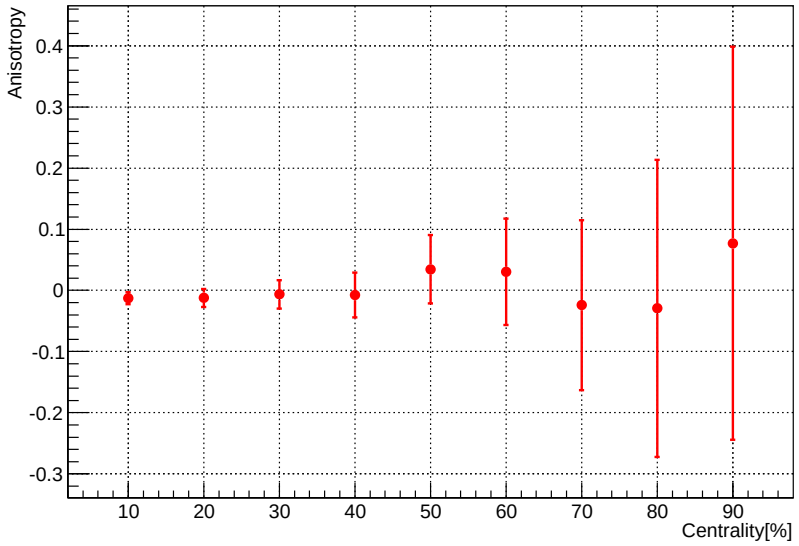

Figure 4.1: Anisotropy ($0.12 \leq M_{ee} \leq 0.3 GeV/c^2$)

4.1.2 Comparison with v2

The azumithal dependence of the particle yield can be described in the form if a Fourier series as follows:

$$E\frac{d^3N}{d^3p} = \frac{1}{2\pi}\frac{d^2N}{p_T dp_T dy}\left(1 + \sum_{n=1}^{\infty} 2v_n(p_T)\cos[n(\phi - \Psi_R)]\right) \qquad (30)$$

where E is the energy of the particle, p the momentum, p_T the transverse momentum, ϕ the azimuthal angle, y the rapidity and Ψ_R the angle of reaction plane.

In order to compare with elliptic flow (v2) and my anisotropy results, calculate the following equation with following two integral region.

$$\int (1 + 2v_2 \cos(2\phi))\, d\phi = \phi + v_2 \sin(2\phi) + Constant \tag{31}$$

The in-plane and out-plane ϕ range are following, respectively.

- $0 \leq \phi \leq \frac{\pi}{4}$, $\frac{3\pi}{4} \leq \phi \leq \frac{5\pi}{4}$, $\frac{7\pi}{4} \leq \phi \leq 2\pi$: the region of Reaction Plane side (RP)
- $\frac{\pi}{4} \leq \phi \leq \frac{3\pi}{4}$, $\frac{5\pi}{4} \leq \phi \leq \frac{7\pi}{4}$: the region of Magnetic Field side (MF)

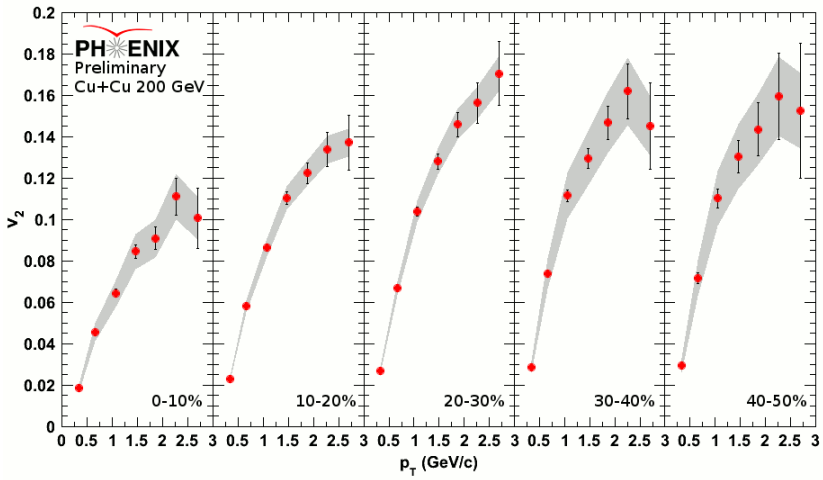

Figure 4.2: Cu+Cu $\sqrt{s_{NN}}$ 200 GeV v2 10% Centrality bins

The both region are integrated by $d\phi$ and calculate the anisotropy.

$$Anisotorpy = \frac{MF - RP}{MF + RP} \tag{32}$$

The v2 value are used the result of hadron elliptic flow at $\sqrt{s_{NN}} = 200$ GeV Cu+Cu in PHENIX as showed in Figure 4.2.

Figure 4.3 shows the comparison with anisotropy. The red dot is the anisotropy results of this thesis and black dot with gray band is the anisotropy calculated by using the values of elliptic flow. These two results are consistent.

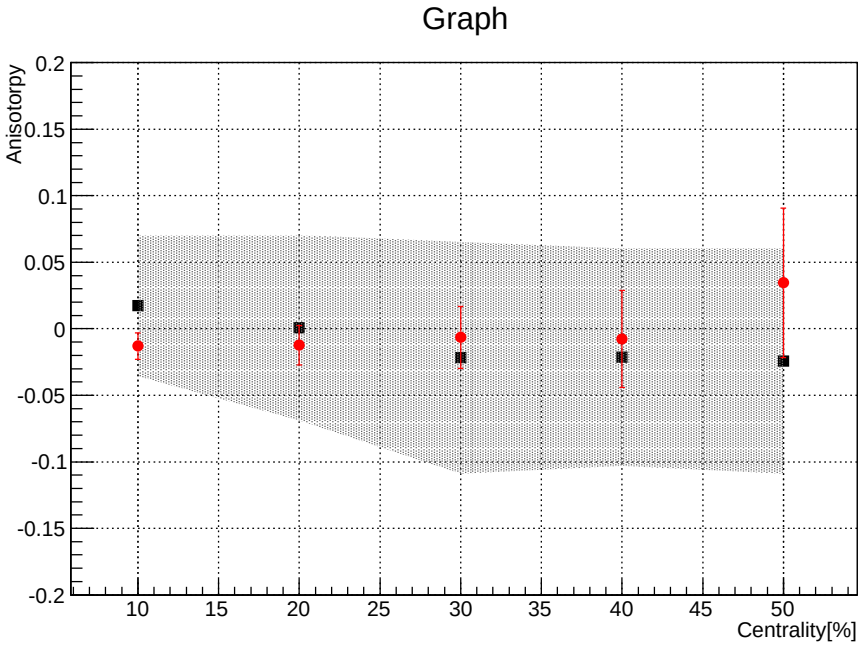

Figure 4.3: Anisotropy comparison

4.2 Polarization

The first measurement of di-electron double ratio of polarization in heavy ion collisions ia showed in Figure 4.4 ($0.12 \leq M_{ee} \leq 0.3 GeV/c^2$). The result of double ratio is consistent with unity in error range.

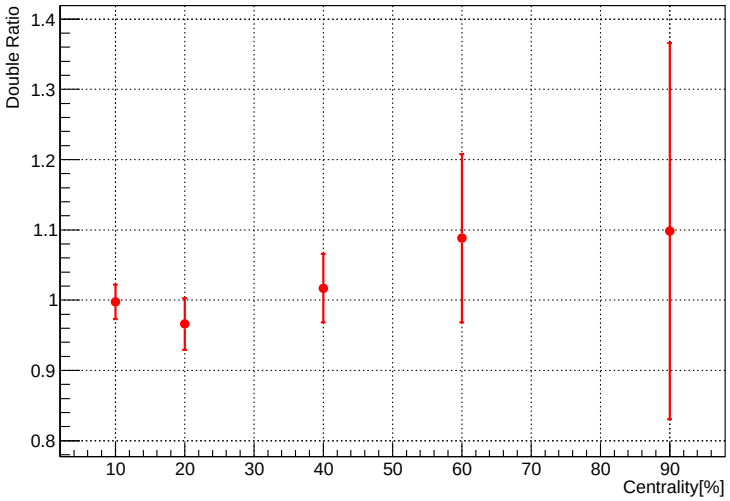

Figure 4.4: Polarization ($0.12 \leq M_{ee} \leq 0.3 GeV/c^2$)

5 Conclusion

We have measured the di-electron anisotropy and polarization for selected centralities in $\sqrt{s_{NN}} = 200$ GeV Cu+Cu collisions.

We identified e^+ and e^- tracks from large other charged particle tracks and reconstructed the invariant mass spectrum of e^+e^- pairs. We selected low mass region, $0.12 < M_{ee} \leq 0.3 GeV/c^2$. This region has about 20% virtual photon component.

At anisotropy measurement, the anisotropy is consistent with zero and it is good agreement with an anisotropy calculated from elliptic flow.

We measured di-electron polarization. This is the first result of di-electron polarization in heavy ion collisions. In order to cancel PHENIX detector acceptance, we used double ratio in order to cancellation of detector acceptance. The double ratio is consistent with unity in statistic error. This measurement did not detect polarization.

We will analyze with Au+Au data which has more statistics than Cu+Cu and we are going to analyze back ground subtraction such as combinatorial and Dallitz decay in order to get virtual photon component. After that, we will measure anisotropy and polarization of virtual photons for the search of the magnetic field.

Acknowledgements

I would like to gratefully acknowledge my superbisor Associate Professor Kenta Shigaki for his support and guidance. I gratefully thank the staff member of Quark Physics Lab. Professor Toru Sugitate and Assistant Professor Kensuke Homma for them great suggestions and advices. I would like to acknowledge Dr. Yasuyuki Akiba and and Dr. Yorito Yamaguchi for them help and good advices.

I would like to thank all PHENIX collaborators. I had a great experience as a PHENIX collaborator and Beam-Beam Counter expert during RHIC Run- 12.

I would like to extend my thanks to M.Nihashi-san and Y.Nakamiya-san. Nihashi-san gave me a great support of my BNL stay. Nakamiya-san taught me detail of electron analysis and discussed with me about my analysis. I also want to thank all students of Quark Physics Lab.

Bibliography

References

[1] J.Rafelski and B. Muller, Phys. Rev. Lett. 36, 517 (1976)

[2] K.Hattori and K.Itakura, hep-ph/1209.2663

[3] P.F.Kolb,Heavy Ion Phys.21,243(2004)

[4] D.E.Kharzeev, L.D.McLerran, and H.J.Warringa, Nucl.Phys.A 803, 227 (2008)

[5] Nuclear Instruments and Methods A 499 (2003) 235 - 244

[6] Nuclear Instruments and Methods A 499 (2003) 423 - 432

[7] BBC Operation at BNL, Quark Physics Lab. web site http://www.hepl.hiroshima-u.ac.jp/phx/bnl/bnl.html

[8] Nuclear Instruments and Methods A 499 (2003) 433 - 436

[9] PHENIX website http://www.phenix.bnl.gov/

[10] Nuclear Instruments and Methods A 499 (2003) 143 - 148

[11] L. Aphecetche et al. (PHENIX Collaboration), PHENIX calorimeter, Nucl. Instr. and Meth. A 499, 521 (2003).

[12] K. Adcox et al. (PHENIX Collaboration), PHENIX central arm tracking detectors, Nucl. Instr. and Meth. A 499, 489 (2003).